Real-Time Rectilinear 3-D Ultrasound Using Receive Mode Multiplexing

Jesse T. Yen and Stephen W. Smith, *Member, IEEE*

***Abstract*—In previous work, we developed two generations of a real-time rectilinear volumetric scanner operating at 5 MHz for abdominal, breast, or vascular imaging using a Mills cross two-dimensional (2-D) array and a rectilinear periodic 2-D array. To improve spatial resolution performance and sensitivity, we developed a new design using 4:1 receive mode multiplexing. With 4:1 multiplexing, the new 65,000 element 2-D array has $4 \times 256 = 1024$ receivers so that 256 receivers can be used on any image line. The two major benefits of using receive mode multiplexing are an increase in receive sensitivity due to a greater number of receive elements, and a decrease in grating lobe and clutter levels due to increased receive element density. Theoretical simulations and analysis show an increase of about 13 dB in sensitivity compared to our previous work. With these encouraging results, a new 65,000 element 5-MHz, 2-D array having 1024 receivers and 169 transmitters was prototyped. In addition, the multiplexer and control circuitry were designed, built, and interfaced with both the transducer and volumetric scanner. Images of tissue-mimicking phantoms and in vivo targets were obtained. Using a spherical cyst phantom, experimental results showed a +12 dB improvement in signal-to-noise ratio and a +6 dB improvement in contrast compared to our previous work.**

I. Introduction

In recent years, both clinical and engineering researchers have been increasingly interested in three-dimensional (3-D) ultrasound imaging. Most methods include some form of mechanical translation of a 1-D array followed by off-line reconstruction [1]. This technology has been developed into a real-time commercial product (Voluson 730, Kretztechnik, Zipf, Austria) wherein multiple B-scans are acquired using a 1-D array mechanically steered in the elevation direction. Several researchers have noted the advantages of such real-time, 3-D ultrasound in obstetric and gynecologic applications, including multiple views and slices not available with 2-D ultrasound, improved accuracy in volume measurement, and volume-rendered images that may aid in the detection of fetal defects [2]. Using these same advantages, visualization using 3-D ultrasound also may improve the detection of breast lesions [3]. In addition, real-time 3-D ultrasound may help clinicians perform ultrasound-guided breast biopsies because the needle no longer has to be perfectly aligned within a single scan plane.

The 3-D ultrasound system used in this work was developed at Duke University and commercialized by Volumetric Medical Imaging (Durham, NC) [4], [5]. Instead of acquiring only a single slice using a 1-D phased array, this system uses a 2-D phased array to acquire an entire volume [6]. Using 16:1 receive mode parallel processing, our transthoracic volumetric system scans a 65° 3-D pyramid with 2-D phased array transducers of approximately 500 active channels to produce 3-D scans at rates up to 60 volumes/seconds. Real-time display options in the 3-D scanner include up to five image planes oriented at any desired angle and depth within the pyramidal volume as well as real-time 3-D volume rendering, 3-D pulse wave Doppler, and 3-D color flow Doppler.

This real-time 3-D ultrasound system has shown promise in cardiac applications. Clinical and animal evaluations have shown potential advantages over conventional 2-D scanners for measurement of cardiac function in terms of ventricular function [7]–[10], detection of perfusion defects [11], reduction of scanning times in dobutamine stress echo exams [12], measurement of peak left ventricular flow velocities [13], guidance of right ventricular endomyocardial biopsy [14], [15], and evaluation of congenital cardiac abnormalities [16].

The subject of this paper is real-time rectilinear 3-D scanning. In typical B-mode imaging with linear arrays, a subset of transducer elements or subaperture is used to send an acoustic beam directly ahead. The subaperture is selected through either multiplexing or turning elements on and off. This subaperture is moved across the entire aperture to form a rectangular scan format [17]. To produce real-time rectilinear 3-D scans, the analogous 2-D linear arrays must have a moving subaperture in two dimensions [17].

To translate the subaperture in a 2-D rectilinear array, three different approaches are possible. The first approach involves no multiplexing of elements. In this approach, the subaperture is moved by turning elements on and off on a line-by-line basis using the software apodization feature of a scanner. No additional hardware is required, and it is the least expensive of the three options. However, using no multiplexing will result in a very sparse array, and only a portion of the available transmit and receive channels are turned on for any given line. A more complex and expensive approach is to use receive mode N:1 multiplexing in which a receive channel may select one element from a group of N elements. Using N:1 multiplexing in receive

Manuscript received April 16, 2003; accepted September 10, 2003. This research was supported by the NIH (grants HL64962 and HL58754) and NSF (grant DMR0104304).

J. T. Yen is with the Biomedical Engineering Department, the University of Southern California, Los Angeles, CA (e-mail: jesse.yen@usc.edu).

S. W. Smith is with the Department of Biomedical Engineering, Duke University, Durham, NC.

0885–3010/$20.00 © 2004 IEEE

mode would increase the receive element density by a factor of N, and a greater number of receivers may be used on any given image line. Meanwhile, the transmit subaperture is still moved by turning elements on and off using apodization. A wide selection of low-voltage (<5 V) multiplexers are commercially available. When choosing a suitable low-voltage multiplexer, several factors including "on" shunt capacitance, "off" shunt capacitance, and "on" resistance should be considered. Because 2-D array piezoelectric elements have low capacitances (3–4 pF), additional shunt capacitances from multiplexers will reduce signal-to-noise ratio (SNR). A high "on" resistance also will reduce SNR. Commercial low-voltage multiplexers such as the MAX4052/A (Maxim Integrated Products, Sunnyvale, CA) have a typical "on" resistance of 60 Ω and "on" and "off" capacitances of 8 pF and 2 pF per channel, respectively.

The last option is to multiplex channels in both transmit and receive modes. This is the most complicated and expensive approach, although using N:1 multiplexing in transmit and receive allows the most flexibility in the design. More expensive high-voltage multiplexers such as the Supertex HV202 (Supertex Inc., Sunnyvale, CA) must be used because they can tolerate the high-transmit voltages (100 V). These high-voltage multiplexers also have "on" and "off" shunt capacitances that degrade SNR. In addition, heating of the multiplexers is a serious concern [18]. Because each approach has different parameters, the optimal sparse 2-D array geometry for one option may not be the optimal geometry for another option. Therefore, each approach may require a different array geometry. Trade-offs between cost, complexity, and image quality must be considered.

In previous work, we developed two versions of a real-time 3-D rectilinear scanner with a 2-D array. The first version used a Mills cross array consisting of two rows of transmit elements and two columns of receive elements in which the multiplicative transmit and receive operation reduced off-axis clutter [6], [17]. This 48,000 element prototype array used 4:1 receive mode parallel processing and had a field of view of $30 \times 8 \times 60$ mm. In addition, we applied the Mills cross design to develop a spherical curvilinear 3-D scanner [19]. This array is analogous to the 1-D curvilinear array commonly used for abdominal and obstetrics applications [17].

In the second version of the rectilinear 3-D scanner, we used a $256 \times 256 = 65,536$ element array and increased the receive mode parallel processing to 16:1, yielding a field of view of $30 \times 30 \times 60$ mm [20]. Notwithstanding these results of the periodic array, the very sparse nature of this array yielded high-grating lobe levels and limited image quality. In this paper, to improve spatial resolution performance and sensitivity, we describe a new design using 4:1 receive mode multiplexing. With 4:1 multiplexing, the new 65,000 element 2-D array has $4 \times 256 = 1024$ receivers so that 256 receivers can be used on any image line. This new multiplexing scheme also uses 16:1 receive mode parallel processing and has a field of view of $30 \times 30 \times 60$ mm. In addition, multiplexer and control circuitry were designed, built, and interfaced with both the transducer and volumetric scanner. Images of tissue-mimicking phantoms and in vivo targets were obtained.

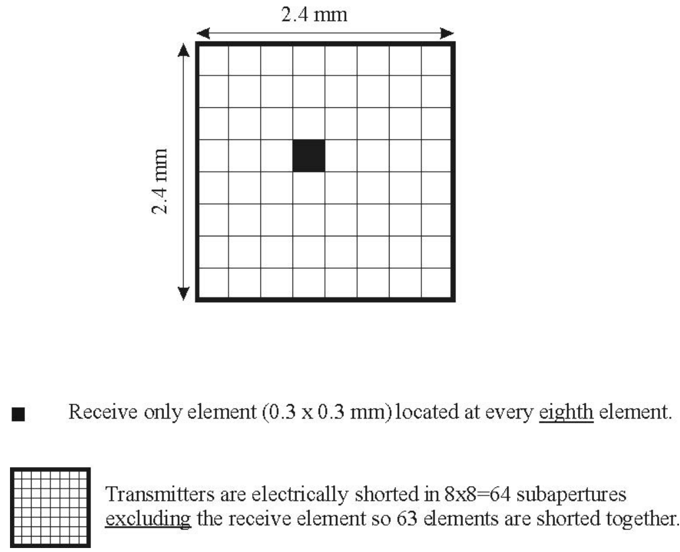

Fig. 1. Schematic of the periodic array. Single cell with a 0.3×0.3 mm receive element and surrounding transmitters.

II. Methods and Materials

A. Array Design

The 2-D array design uses a sparse periodic pattern. In Figs. 1–4, we compare our previous periodic design (Figs. 1 and 2) [20] with the new pattern (Figs. 3 and 4). Previously, we repeated a single cell consisting of a small receive element embedded in a large transmit "piston". A schematic of the single cell is shown in Fig. 1 and the entire array demonstrating the moving subapertures is shown in Fig. 2. In the new design, instead of having only one receive element, each cell has four receive elements. Our initial simulations with symmetric periodic layouts showed unacceptably high grating lobe levels near the main beam. Therefore, multiple asymmetric periodic layouts fitting our design constraints were studied. Other researchers also have explored similar sparse periodic layouts with either symmetric or asymmetric periodicity with the intention of reducing clutter [21], [22]. Starting with a symmetric periodic layout, elements then were displaced $\pm 2\lambda = 0.6$ mm in either azimuth or elevation to achieve an asymmetric layout. The beamplots of these new 2-D array layouts with staggered patterns were investigated in Field II [23]. Ultimately, the pattern in Fig. 3 gave the best performing beamplot in terms of clutter and grating lobe levels. In this pattern, any remaining elements not chosen to be a receive element within the cell becomes a transmit element. All transmit elements in a 2.4 mm $\times$ 2.4 mm square are shorted together, essentially forming a transmit "piston" because transmit focusing is not used for receive mode parallel processing. With

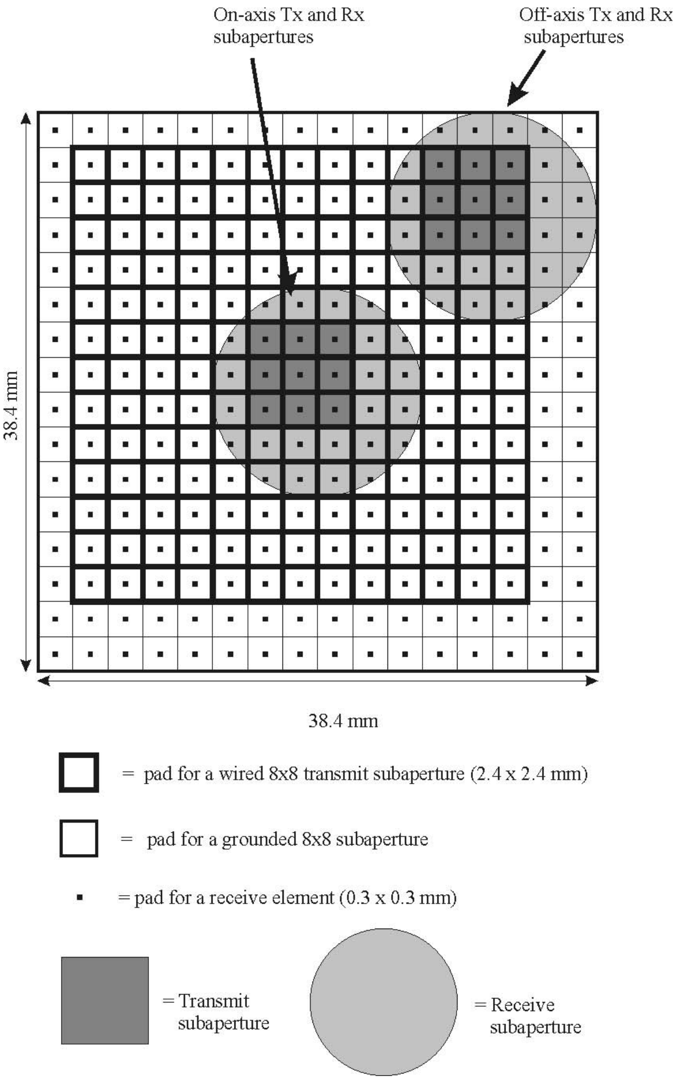

Fig. 2. Schematic of the entire array showing on-axis and off-axis subapertures for transmit (dark shading) and receive (light shading).

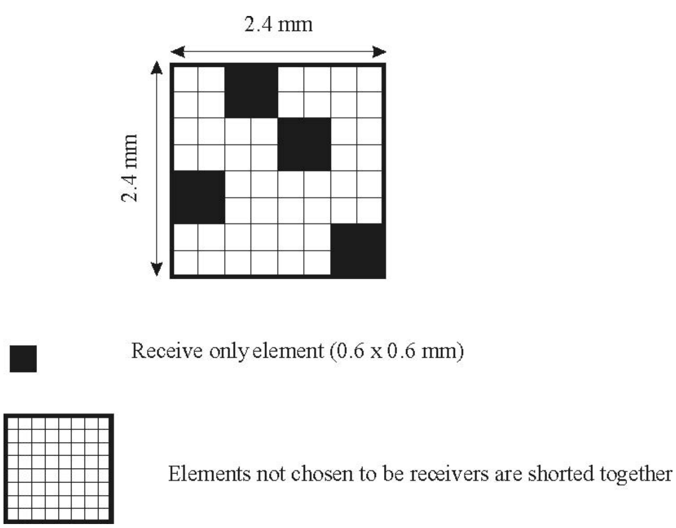

Fig. 3. Schematic of the multiplexed array. Single cell with 0.6×0.6 mm receive elements and surrounding transmitters.

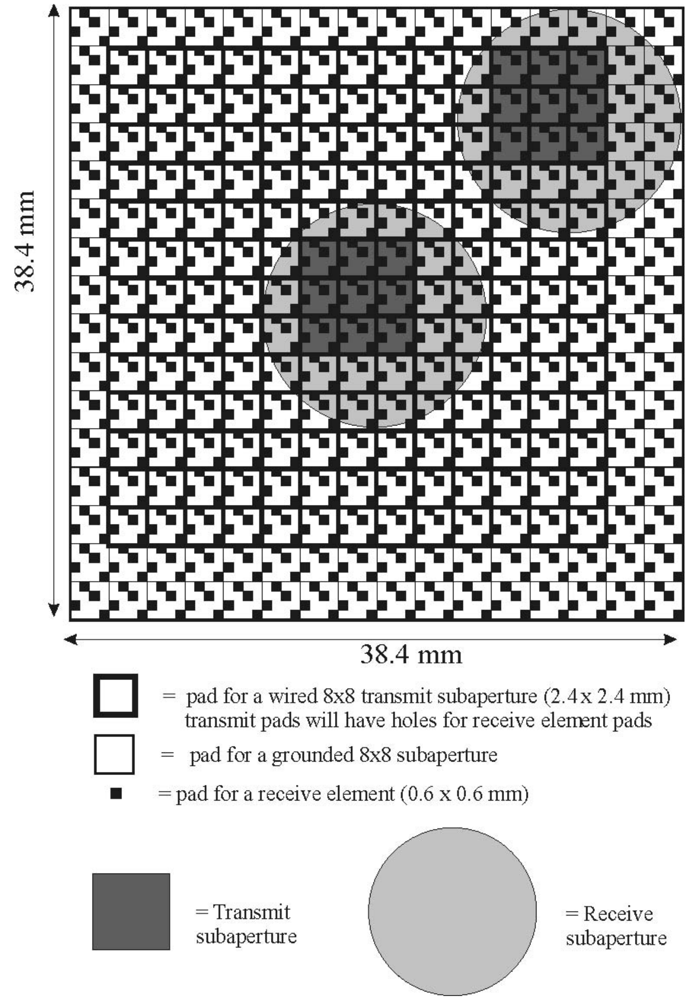

Fig. 4. Schematic of the entire array showing on-axis and off-axis subapertures for transmit (dark shading) and receive (light shading).

4:1 receive multiplexing, we then have $4 \times 256 = 1024$ receivers. In this design, each receive element had dimensions of 600 μm $\times$ 600 μm. Fig. 3 shows a single cell of the periodic array in which the black squares indicate receive elements and the remaining elements are transmit. Fig. 4 is a schematic of the entire 128×128 array showing selected transmit and receive subapertures for the image lines at (x,y,z) = (0,0,30) mm and (x,y,z) = (13,13,10) mm. The $13 \times 13 = 169$ large transmit elements, outlined in a thicker line, were used because our handle can connect a maximum of 184 transmitters. The outer transmit elements, shown in a thinner line, are grounded because they are never used. The four elements from each multiplexer available to any scanner receive channel are offset by 19.2 mm in both x and y dimensions. For example, if an element has a location (x,y) = (−9.6,−9.6) mm, then the remaining three element locations addressed by the multiplexer are (−9.6,9.6), (9.6,−9.6), and (9.6,9.6) mm.

B. Simulations

Computer simulations using Field II software [23] were calculated to compare a "gold standard" fully sampled

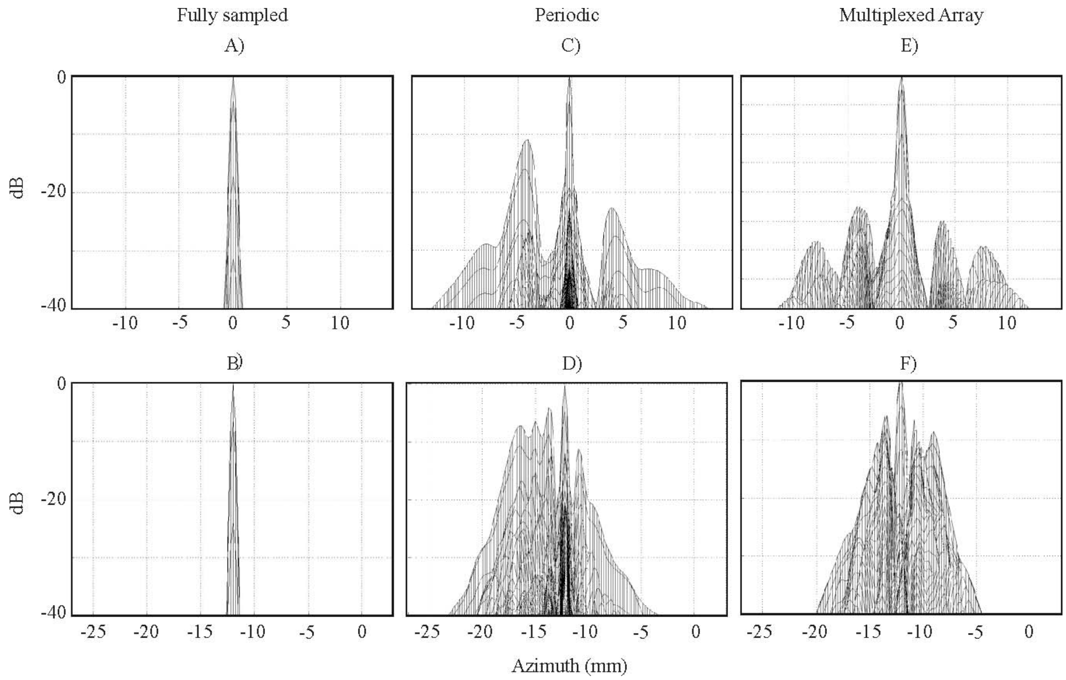

Fig. 5. Simulated on-axis and off-axis beamplots for the fully sampled array, periodic array, and multiplexed array. (A) On-axis (x,y,z) = (0,0,30) mm fully sampled array. (B) Off-axis (x,y,z) = (13,13,10) mm fully sampled array. (C) Periodic array focused on-axis. (D) Periodic array focused off-axis. (E) Multiplexed array focused on-axis. (F) Multiplexed array focused on off-axis.

TABLE I
Summary of Simulation Results of the Three Arrays.

	Fully sampled		Periodic		4:1 Mux	
	On-axis	Off-axis	On-axis	Off-axis	On-axis	Off-axis
Number of transmit elements used	4097	441	567	567	432	432
Number of receive elements used	4097	441	120	12	256	54
Pulse-echo sensitivity (dB)	0	−19	−47	−56	−34	−41
−6 dB beamwidth (mm)	0.564	0.564	1.026	1.983	0.706	1.806
−20 dB beamwidth (mm)	1.107	1.108	5.955	8.426	1.433	5.093
−40 dB beamwidth (mm)	1.778	1.781	25.805	19.805	12.135	11.323

array ($128 \times 128 = 16,384$ elements) versus the previous periodic array design and the new periodic design with multiplexing. For each array, the on-axis beamplot (x,y,z) = (0,0,30) mm and an off-axis beamplot (x,y,z) = (13,13,10) mm are shown in Fig. 5. F#=1 apertures were used for each beamplot, and data is displayed over a 40-dB dynamic range. The left column shows on-axis and off-axis beamplots for the fully sampled array [Fig. 5A and B]. The main beam is very narrow down to −40 dB. In the middle column, on-axis and off-axis beamplots for the previous periodic array are shown [Fig. 5C and D] [20]. Due to the sparseness, the highest grating lobe level is −9 dB for the on-axis case. These grating lobes are located at ±4 mm. Because the center of the transmit subaperture is not directly over the receive mode focus, there is an asymmetry in the grating lobe levels. The on-axis and off-axis beamplots for the multiplexed array are shown in the right column [Fig 5E and F]. The highest grating lobe level is −22 dB, a 13 dB decrease compared to the periodic array. In Table I, the number of elements in transmit and receive, pulse-echo sensitivities normalized to 0 dB for the fully sampled array focused on-axis, and the −6 dB, −20 dB, and −40 dB beamwidths are compared for each array. The number of elements recorded in Table I was determined by counting the number of 300 μm × 300 μm elements used in each transmit and receive subaperture. Note that the pulse-echo sensitivity of the multiplexed array focused on-axis is 13 dB higher compared to the periodic array.

C. Flex Circuit Design

A multilayer, flexible, interconnect circuit for the periodic array was fabricated by Microconnex (Snoqualmie, WA) as previously described by Fiering *et al.* [24]. A photograph of the flex circuit is shown in Fig. 6. The array is located in the center of the flex circuit, and the ends of the flex have solder pads for making connection to our volumetric scanner. The array area was 38.4 × 38.4 mm. Routing of the $13 \times 13 = 169$ transmitters is distributed

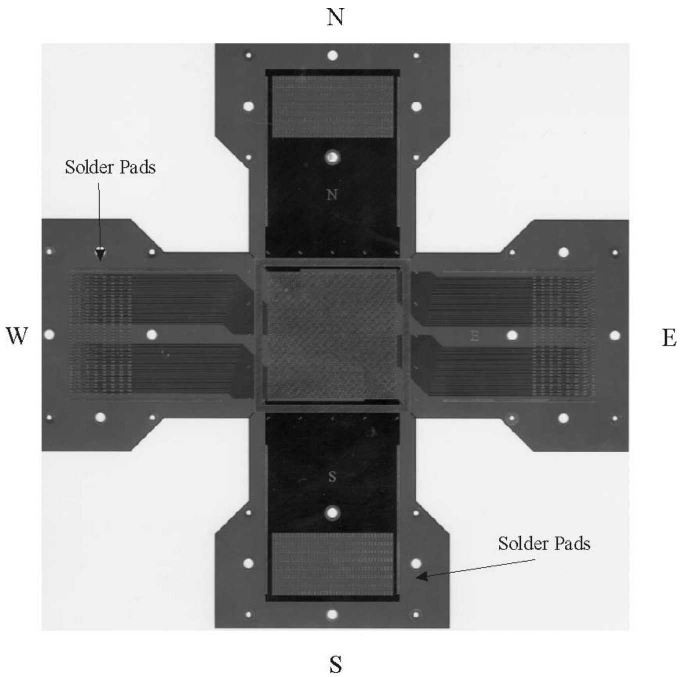

Fig. 6. Photograph of flexible interconnect circuit. The entire circuit with solder pads.

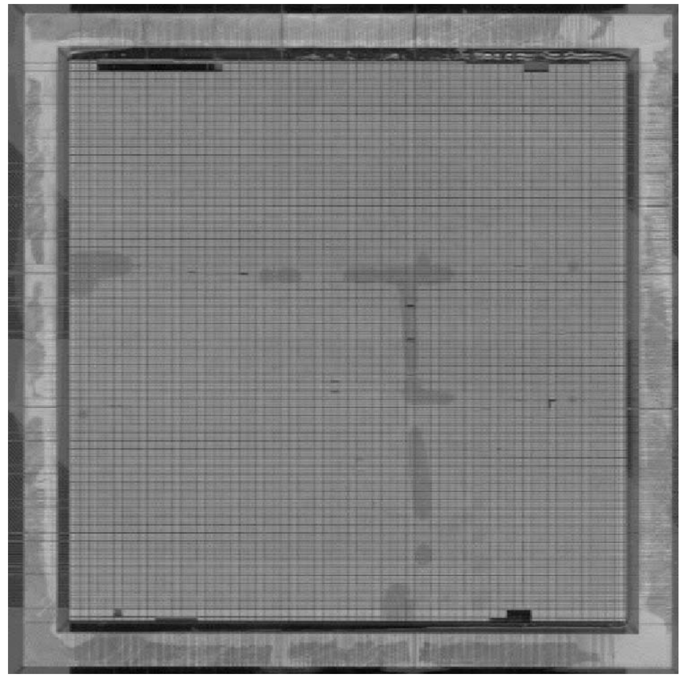

Fig. 7. Photograph of close-up of the array after dicing.

among the four wings such that the north, west, south, and east wings have 48, 48, 37, and 36 transmitters, respectively. Each wing also contains gold pads for 256 receivers. These receivers were the inputs to 32 dual 4:1 multiplexers MAX4052/A (Maxim Integrated Products, Sunnyvale, CA). There were alignment holes in the corners of each wing for 1/16-in. diameter steel dowel pins. On the sides of the wings, we used 3/4-in. 4–40 screws to clamp the flex circuit to the multiplexer printed circuit board (PCB). Using an alignment device consisting of a steel plate and steel dowel pins, we properly aligned and clamped the flex circuit to the multiplexer PCB.

D. Transducer Fabrication

A 40 mm $\times$ 40 mm $\times$ 0.288 mm wafer of PZT-5H (CTS Wireless, Albuquerque, NM) was attached to the multilayer, flexible, interconnect circuit using a thin film bond of nonconductive epoxy. Afterward, the PZT was diced in both directions at a pitch of 600 μm, using a 25 μm diamond-dicing blade. The kerf was 35 μm due to blade wobbling and dulling. All of these elements were then partially subdiced at a pitch of 150 μm with a kerf depth of 200 μm to suppress lateral modes. A close-up of the completed diced array containing over 65,500 elements is shown in Fig. 7. After dicing, a 50 mm $\times$ 50 mm $\times$ 0.008 mm sheet of silver foil was bonded to the top of the array to ground the elements. A 9-mm thick, lossy epoxy backing consisting of 30 g of tungsten oxide (Cerac Specialty Inorganics, Milwaukee, WI), 5.25 g of LP-3 (Morton International, Chicago, IL), 1.125 g of phenolic balloons (Union Carbide, Danbury, CT), 3.0 g of Zeeospheres (3M, St. Paul, MN), 9.75 g of Dow Epoxy Resin 332 and 3.375 g Dow Epoxy Hardener 24 (Dow Chemical Company, Midland, MI) was cast onto the flex behind the transducer. No matching layer was included in this prototype array because of the large size of the PZT chip. The Krimholtz-Leedom-Matthei (KLM) simulations were used to predict the performance of an individual array element in terms of electrical impedance, impulse response, and power spectrum [25]. Experimental vector impedance and pitch-catch measurements were made for this array.

E. Multiplexer Board Design

For the multiplexers, we used the MAX4052/A dual 4:1 multiplexer. After an extensive search, this multiplexer had the best balance between “on”/“off” capacitance and “on” resistance, which are factors that may reduce SNR. The output of the multiplexer is loaded with a cable capacitance of 48 pF and a preamplifier input impedance of 22 k$\Omega \parallel$ 60 pF. Each board contained 32 dual 4:1 multiplexers and a control device. Each multiplexer required two control bits to select between four inputs. Power supply voltages for the multiplexer were set to +5 V and −5 V. The control device was a Xilinx (San Jose, CA) XCR256XL-TQ144 complex, programmable, logic device (CPLD). These devices were in-system programmable via a joint test action group (JTAG) cable. To synchronize the CPLD with the volumetric scanner, the CPLD received a clock signal indicating the start of a transmit line and a reset signal indicating the start of a new volume from the volumetric scanner. Based on these two signals, the CPLD had a lookup table (LUT) containing the proper control bits for the 32 multiplexers on that board for every transmit line. The CPLD was programmed using verilog hardware description language (VHDL). The CPLD

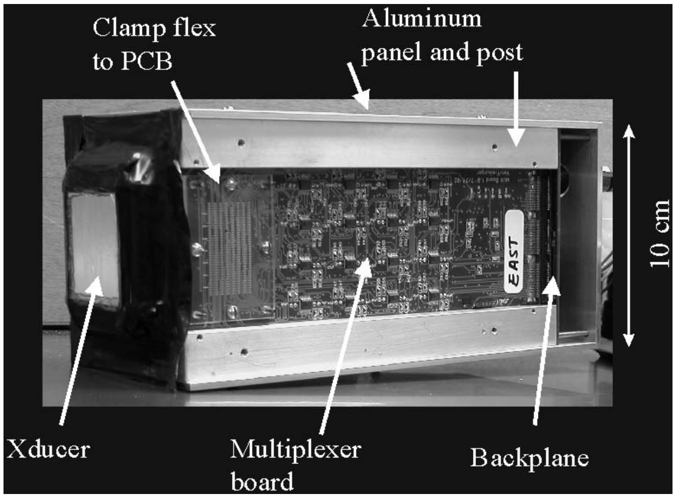

Fig. 8. Photograph of the assembled multiplexed transducer, which includes the transducer, multiplexer board, backboard, and aluminum housing.

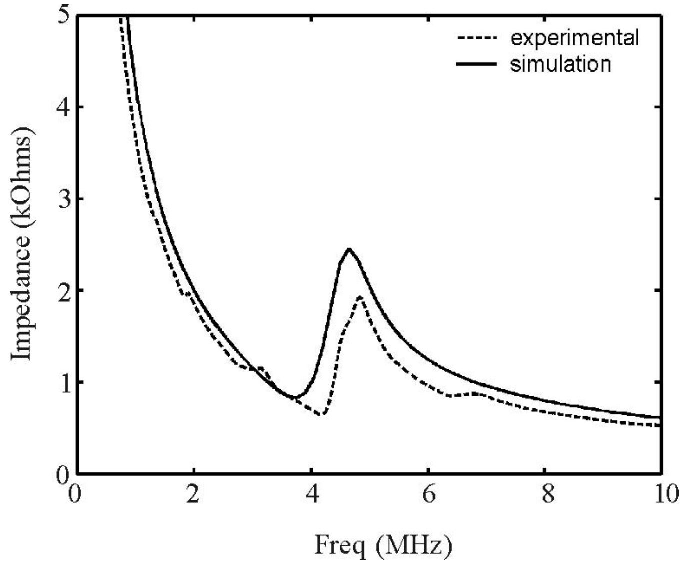

Fig. 9. Simulated and experimental results of individual elements. Simulated (—) and experimental (---) vector impedance measurement of a receive element.

supply voltage was set to +3.3 V. The board also had corresponding alignment and screw holes for the clamp. On the other end, there was a 150-pin edge-mount connector with a pin pitch of 0.635 mm (Part. No. QTS-EM-075-01-L-D-EM2 Samtec, New Albany, IN). The multiplexer board schematic and layout was designed using P-CAD 2001 (Altium Limited, San Diego, CA) software along with the SPECCTRA (Cadence Design Systems, San Jose, CA) autorouter program. This board had 10 layers consisting of six trace layers, two ground planes, and two power planes. One of the power planes was used for −5 V, and the other power plane was split to provide both +5 V and +3.3 V.

F. Backboard Design

The backboard had the mating Samtec connector (Part. No. QTS-075-01-L-D-A). On the back of the backboard, we had solder pads to solder leaves that connect to the transducer handle of the volumetric scanner. The backboard also had two coaxial connectors for the timing signals from the volumetric scanner. The backboard was a 10-layer board having six trace layers, two ground planes, and two power planes where one of the power planes is split to supply both +5 V and +3.3 V. Both the multiplexer board and backboard were fabricated by PCSM (Printed Circuit Solutions Manufacturing, Galax, VA). All components were hand-soldered. Power to the multiplexers (±5 V) and CPLD (+3.3 V) on all four boards was delivered through the Samtec connectors. The total assembly—consisting of the transducer, multiplexer board, backboard, and aluminum housing—is shown in Fig. 8. The dimensions are $10 \times 10 \times 20$ cm, and it weighs 3.06 kg.

G. Beamformer Modifications

The original delay program, written in the C programming language, calculates delays for 512 transmit channels and 256 receive channels. The delay program was modified to accommodate the 1024 receive elements available. In receive, the delay program selected the closest among four elements to the focus among the four available elements for each channel, then calculated the delay based on the distance between the element position, focus, and speed of sound. The delay program also recorded which one of the four elements was selected for every receive channel on every transmit line. After the delay calculations, this information was written to four VHDL files used to program the corresponding CPLDs.

III. Results

A. Transducer Testing

Experimental impedance measurements of a receive element (---) compared to simulation (—) are shown in Fig. 9. Due to blade wobbling and dulling, the diced elements had dimensions of 565 μm $\times$ 565 μm with a 35 μm kerf. Each element was partially subdiced at a 150 μm pitch in both dimensions. The subdicing kerfs reduced the effective area to 400 μm $\times$ 400 μm. The KLM simulations of a receive element showed a series resonance of 830 Ω at 3.9 MHz. Typical experimental vector impedance measurements (Hewlett-Packard HP4194A Impedance/Gain-Phase Analyzer, Palo Alto, CA) showed a series resonance of 650 Ω at 4.2 MHz. The series and parallel resonance in both experiment and simulation showed good agreement with each other. Because the KLM model is a 1-D model, it does not take into account the effects of partial subdicing, which may account for the differences between simulated and experimental results. In our 1-D KLM model, the subdicing was taken into account by using a smaller effective area that would increase the electrical impedance. The effective area entered into our model was the sum

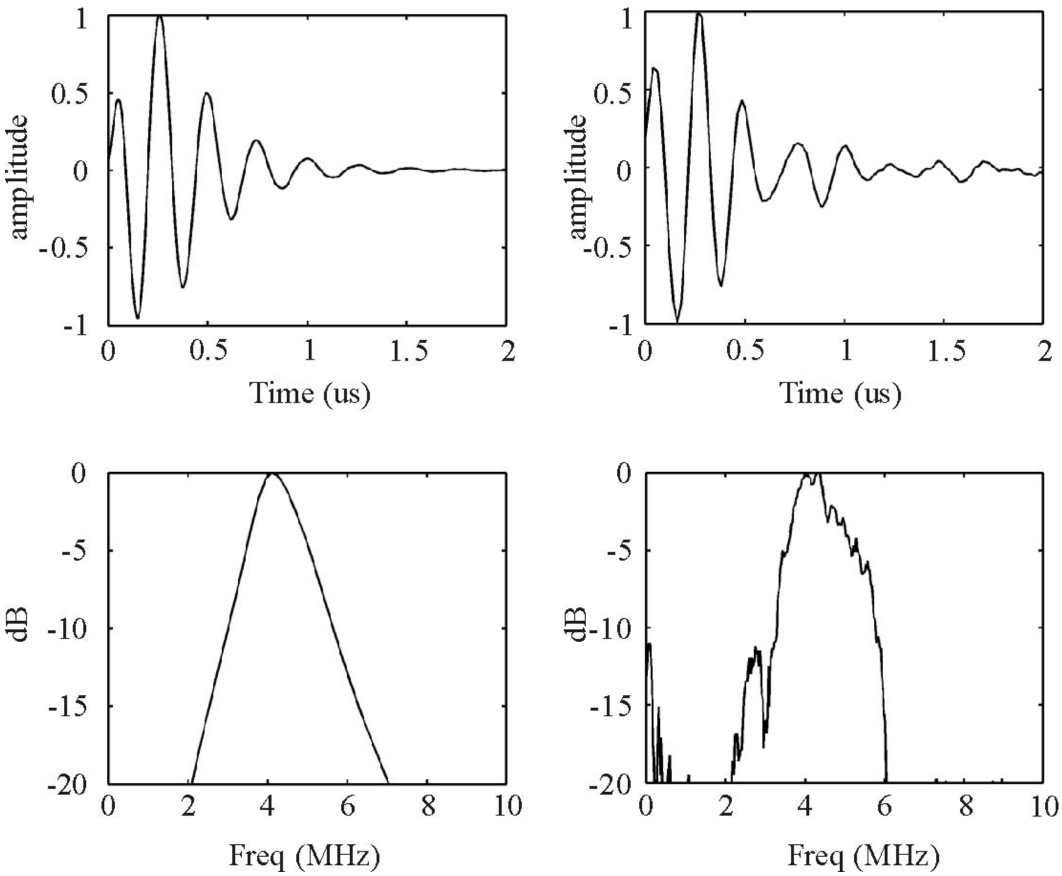

Fig. 10. Simulated and experimental pulses and spectra from a pitch-catch measurement. Left column is the pulse and spectrum from KLM. The right column is the experimental pulse and spectrum.

total of our individual elements assuming complete subdicing cuts through the PZT. However, only a partial subdicing was done, which cannot be accounted for in a 1-D model. Therefore, the simulated impedance was slightly higher than the experimental impedance. Also, a partially subdiced element would have less of a downshift in the center frequency versus a completely subdiced element. This may account for the higher center frequency in the experimental pitch-catch response.

Pitch-catch KLM simulations predict a response with a center frequency of 4.3 MHz and a −6-dB fractional bandwidth of 42% (Fig. 10). Pitch-catch measurements of individual elements were made in a water tank to measure impulse response and power spectrum using an oscilloscope (Tektronix TDS 744A, Wilsonville, OR) and spectrum analyzer (Hewlett-Packard HP3588A, Everett, WA). The signal from the spectrum analyzer was not averaged. In this experiment, one large transmitter was excited using a Panametrics 5073PR pulser/receiver (Waltham, MA), and a nearby smaller receive element was chosen to be a receiver. An aluminum block was placed about 3 cm away from the transducer. The transducer and aluminum block were rotated to give the strongest receive signal. A typical experimental pulse and spectrum and simulated pulse and spectrum are shown in Fig. 10. The experimental pulse had a center frequency of 4.5 MHz and a −6-dB fractional bandwidth of 45%.

Transmit element yield was determined by firing each transmit "piston" individually. A 5-MHz Panametrics (Waltham, MA) piston was used as a receiver. If no echoes were received, the transmitter was assumed to be a "dead" element. To determine receive element yield, the same 5-MHz Panametrics (Waltham, MA) piston was used as a transmitter, and echoes from individual receive elements were received at the output of the multiplexers. The receiver was counted as a "dead" element if no echoes were received at the output. The completed array yielded 89.3% working transmitters and 91.3% working receivers. The dysfunctional transmitters and receivers were randomly distributed throughout the aperture. Possible causes include defects in the flex circuit, poor electrical contact between the flex and PZT, and poor contact between the PZT and ground foil.

An experimental system response from a point target was obtained using the volumetrics scanner as an approximate comparison with the simulated transducer beamplot. A 400-μm diameter steel sphere embedded into a 2 cm $\times$ 9 cm US gel pad (Parker Laboratories, Fairfield, NJ) served as a point target. A lateral beam plot was obtained from the C-scan of the acquired volume. Fig. 11 shows an experimental on-axis beamplot (---) with a focus at (x,y,z) = (0,0,30) mm. A new simulated on-axis beamplot was calculated (—) using Field II to take into account various system factors. These factors include a clock fre-

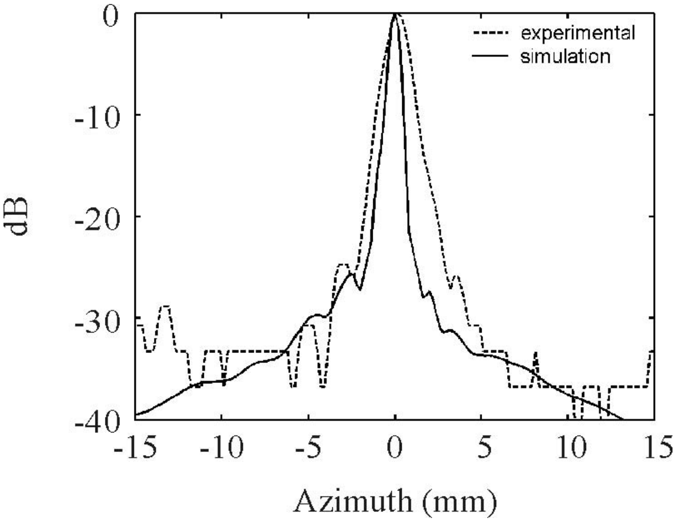

Fig. 11. Simulated (—) and experimental (---) on-axis system point target response of the multiplexed array.

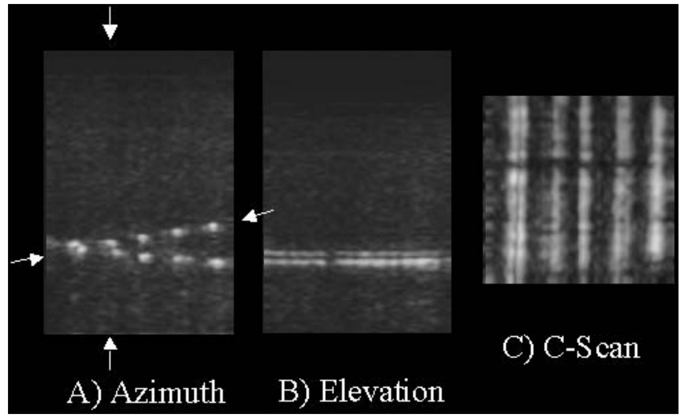

Fig. 12. Orthogonal simultaneous B-scans and a C-scan of wire targets with axial separation distance of 0.5, 1, 2, 3, and 4 mm (from left to right). (A) The azimuth B-scan shows the wires in cross section. (B) The elevation B-scan shows the pair of wires with 1 mm of separation. (C) The C-scan shows the top set of wires. Vertical and tilted arrow pairs show the location of the elevation B-scan and C-scan, respectively, relative to the azimuth B-scan.

quency (40 MHz) for sampling and delay quantization. The one-way element directivity was assumed to have the form $[\mathrm{sinc}(x)]\cos\theta$ where $x = (\pi a/\lambda)\sin\theta$ and a is the element width. Because the tests were done in a water tank, the sound speed was near 1470 m/s, but the assumed sound speed of the scanner and the simulation was 1540 m/s. A random apodization was included to simulate the variation in element sensitivity. The downloaded experimental pulse from a pitch-catch experiment was used in our simulation. However, the effects of receive mode parallel processing were not included in the simulation. The system response included 16:1 receive mode parallel processing with 16 simultaneous receive beam locations for each transmit beam. Both the simulated and experimental were normalized to 0 dB. At -6 dB, the beamwidths were 1.746 mm and 0.849 mm for the experimental and calculated results, respectively. At -20 dB, the widths were 4.211 and 2.347 for the experimental and calculated results, respectively. The average clutter level was -35 dB for the experimental plot. The main beam of the calculated beam plot is narrower than the experimental, as expected, due to the fact that parallel processing was not accounted for in the simulation.

B. Images

Figs. 12–15 show real-time rectilinear images of various targets using the new multiplexed array and the modified volumetric Model 1 scanner. All images in the following figures have a 30×30 mm field of view in azimuth and elevation. The scan depth varies according to target location. Vertical arrows in the azimuth B-scan show the location of the elevation B-scan, and horizontal arrows show the location of the C-scan. Fig. 12 shows wire targets in a tissue-mimicking phantom (CIRS Model 40, Norfolk, VA). The azimuth scan shows the wires in cross section (Fig. 12A), and the perpendicular elevation B-scan shows the pair of wires separated by 1 mm (Fig. 12B). The tilted C-scan

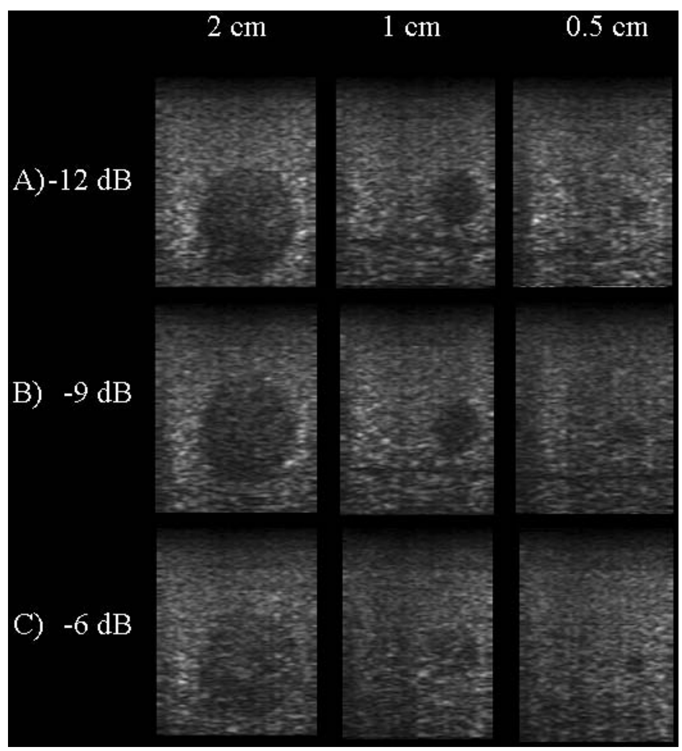

Fig. 13. Collage of B-scans of 2 cm, 1 cm, and 0.5 cm diameter cylindrical cysts with contrasts -12, -9, and -6 dB in rows A, B, and C, respectively.

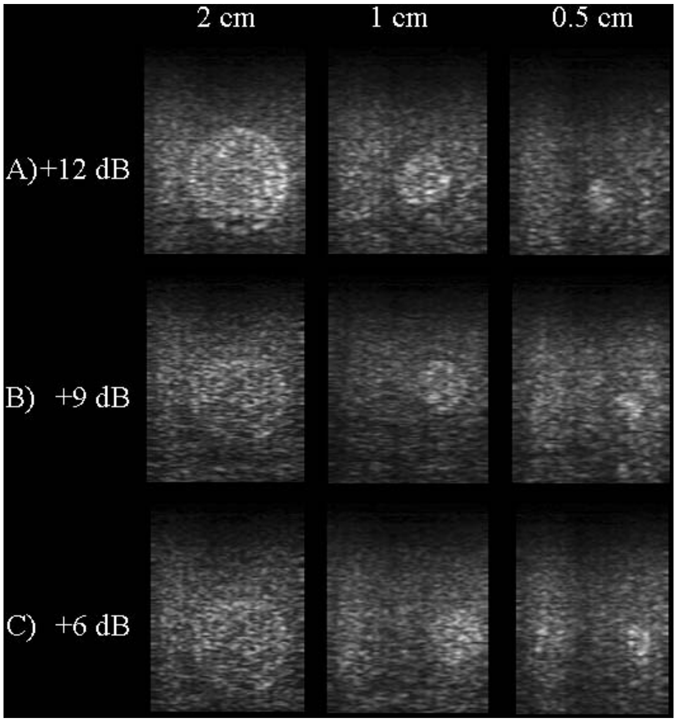

Fig. 14. Collage of B-scans of 2 cm, 1 cm, and 0.5 cm diameter cylindrical tumors with contrasts +12, +9, and +6 dB in rows A, B, and C, respectively.

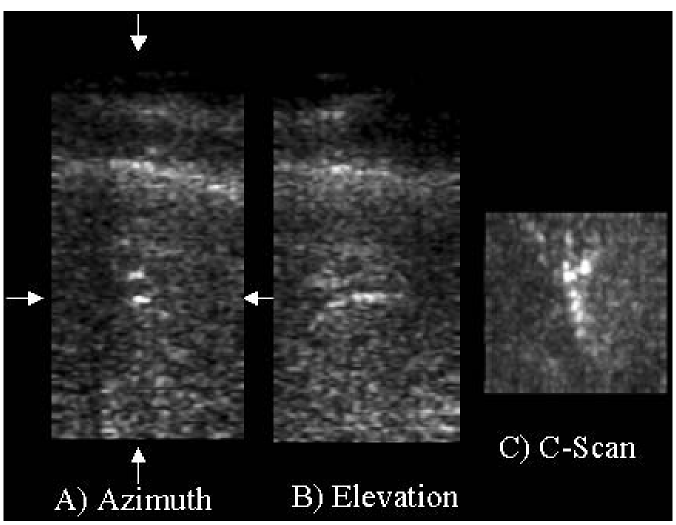

Fig. 15. B-scans and C-scan of a hepatic vessel from a normal volunteer. (A) The vessel is shown in cross section in the azimuth B-scan. (B) The long-axis is shown in the elevation B-scan. (C) The vessel wall is shown in the C-scan. Vertical and horizontal arrow pairs show the location of the elevation B-scan and C-scan, respectively, relative to the azimuth B-scan.

shows the top row of wires with a lateral separation of 5 mm (Fig. 12C).

Fig. 13 is a collage of real-time B-scans showing cross-sectional images of three different contrast cysts in a tissue-mimicking contrast detail phantom (ATS Laboratories, Bridgeport, CT, Model 532B) [26]. Each cyst is in the shape of a stepped cylindrical cone with three different diameters: 2, 1, and 0.5 cm. Three sets of images correspond to different contrast cysts. From top to bottom, the cysts are −12, −9, and −6 dB darker than the surrounding media, and the cyst diameters vary from 2, 1, and 0.5 cm going from left to right. The 2-cm diameter cysts are easily detectable for all three contrast levels. The smaller lesions with less contrast also can be identified, although they are slightly more difficult to detect.

Fig. 14 is a collage of real-time B-scans showing cross-sectional images of three different contrast tumors in the contrast-detail phantom. Similar to the cysts, each tumor is in the shape of stepped cylindrical cone with three different diameters: 2, 1, and 0.5 cm. From top to bottom, the tumors are +12, +9, and +6 dB brighter than the surrounding media, and the diameters vary from 2, 1, and 0.5 cm going from left to right. All tumors are readily detectable.

In another experiment, the B-scans of a 1.5-cm diameter spherical cyst (contrast = −20 dB) (University of Wisconsin phantom, Madison, WI) were analyzed using both the multiplexed array and the previous periodic array. For the multiplexed array, the average increase in brightness was 12 dB over the previous periodic array compared to our calculated 13-dB improvement, and the average contrast of the cyst increased by 6 dB.

Fig. 15 shows an in vivo hepatic blood vessel from a normal 43-year-old male volunteer using a 5-cm scan depth. The cross section of the vessel can be seen in the azimuth B-scan at a 3-cm depth (Fig. 15A), and the long axis can be seen in Fig. 15B. The tilted C-scan shows the vessel wall (Fig. 15C).

IV. Summary

We developed a real-time, 3-D rectilinear scanner using a 4:1 receive mode multiplexing with a 2-D array containing over 65,500 elements to improve the image quality compared to that of our previous periodic array. Operating at 5 MHz, this multiplexed array uses 1024 receive elements, a factor of four increase over our previous periodic array. For real-time rectilinear volumetric imaging, we used large transmit elements (2.4 mm × 2.4 mm) because neither steering nor focusing is essential in transmit. Transmit steering is not necessary in rectilinear 3-D imaging because each transmit beam is fired perpendicular to the transducer face. Transmit focusing is not essential either because a wide transmit is desirable for receive mode parallel processing. Because neither transmit steering nor focusing capabilities are necessary, significant reduction in the design complexities can be made. For dynamic focusing in receive mode, subdiced receive elements (0.575×0.575 mm) were periodically spaced throughout the entire array. These receive elements are staggered in both azimuth and elevation dimensions to suppress grating lobe levels. According to our simulations, we achieved a 13-dB increase in pulse-echo sensitivity and a 13-dB decrease in grating lobe levels when comparing the performance of the previous periodic array and multiplexed array. Comparisons between simulated and experimental transducer performance and beamplots showed reasonably good agreement given the limitations of our computer models. Images of a cyst in a tissue-mimicking phantom showed improved image quality over the previous periodic array. However, side-by-side images were not included because the cyst is not visible using the previous periodic array under the same system settings used on our new multiplexed array. Wire targets with varying axial resolution show that wires with a 1-mm axial separation could be distinguished. A contrast detail study showed that 5-mm diameter cysts and tumors with −6 dB contrast could be detected. Real-time images of an in vivo hepatic blood vessel were shown.

Acknowledgments

The authors thank Ned Light for helpful conversations on transducer fabrication, Mark Freiburger, and John Castellucci for help with the PCB designs, and Christine Merdes for her assistance with the Xilinx CPLDs.

References

[1] A. Fenster and D. B. Downey, "3-D ultrasound imaging: A review," *IEEE Eng. Med. Biol.*, vol. 15, pp. 41–51, Nov. 1996.

[2] D. Pretorious, N. N. Borok, M. S. Coffler, and T. R. Nelson, "Three-dimensional ultrasound in obstetrics and gynecology," *Radiol. Clin. N. Amer.*, vol. 39, no. 3, pp. 499–521, May 2001.

[3] M. Lanfranchi, *Breast Ultrasound*. New York: Marban Books, 2000, pp. 273–275.

[4] S. W. Smith, H. E. Pavy, and O. T. von Ramm, "High speed ultrasound volumetric imaging system. Part I: Transducer design and beam steering," *IEEE Trans. Ultrason., Ferroelect., Freq. Contr.*, vol. 38, pp. 100–108, 1991.

[5] O. T. von Ramm, S. W. Smith, and H. E. Pavy, "High speed ultrasound volumetric imaging system. Part II: Parallel processing and display," *IEEE Trans. Ultrason., Ferroelect., Freq. Contr.*, vol. 38, pp. 109–115, 1991.

[6] J. T. Yen, J. Steinberg, and S. W. Smith, "Sparse 2-D array design for real-time rectilinear volumetric imaging," *IEEE Trans. Ultrason., Ferroelect., Freq. Contr.*, vol. 47, pp. 93–110, 2000.

[7] M. A. Schmidt, C. J. Ohazama, K. O. Agyeman, R. Z. Freidlin, M. Jones, J. M. Laurienzo, C. L. Brenneman, A. E. Arai, O. T. von Ramm, and J. A. Panza, "Real-time three-dimensional echocardiography for measurement of left ventricular volumes," *Amer. J. Card.*, vol. 84, pp. 1434–1439, 1999.

[8] J. X. Qin, M. Jones, T. Shiota, N. L. Greenberg, H. Tsujino, M. S. Firstenberg, P. C. Gupta, A. D. Zetts, Y. Xu, J. P. Sun, L. A. Cardon, J. A. Odabashian, S. D. Flamm, R. D. White, J. A. Panza, and J. D. Thomas, "Validation of real-time three-dimensional echocardiography for quantifying left ventricular volumes in the presence of a left ventricular aneurysm: In vitro and in vivo studies," *J. Amer. Coll. Cardiol.*, vol. 36, pp. 900–907, 2000.

[9] T. Irvine, G. D. Stetten, V. Sachdev, A. Zetts, M. Jones, Y. Mori, C. Ramsperger, J. Castellucci, A. Kenny, J. Panza, O. von Ramm, and D. Sahn, "Quantification of aortic regurgitation by real-time 3-dimensional echocardiography in a chronic animal model: Computation of aortic regurgitant volume as the difference between left and right ventricular stroke volumes," *J. Amer. Soc. Echocardiog.*, vol. 14, no. 11, pp. 1112–1118, 2001.

[10] J. X. Qin, T. Shiota, H. M. Lever, D. N. Rubin, F. Bauer, Y. J. Kim, M. Sitges, N. L. Greenberg, J. K. Drinko, M. Martin, D. A. Agler, and J. D. Thomas, "Impact of left ventricular outflow tract area on systolic outflow velocity in hypertrophic cardiomyopathy—A real-time three-dimensional echocardiographic study," *J. Amer. Coll. Cardiol.*, vol. 39, no. 2, pp. 308–314, 2002.

[11] G. Camarano, M. Jones, R. Z. Freidlin, and J. A. Panza, "Quantitative assessment of left ventricular perfusion defects using real-time three-dimensional myocardial contrast echocardiography," *J. Amer. Soc. Echocardiog.*, vol. 15, no. 3, pp. 206–213, 2002.

[12] M. Ahmad, T. R. Xie, M. McCulloch, G. Abreo, and M. Runge, "Real-time three-dimensional dobutamine stress echocardiography in assessment of ischemia: Comparison with two-dimensional dobutamine stress echocardiography," *J. Amer. Coll. Cardiol.*, vol. 37, pp. 1303–1309, 2001.

[13] H. Tsujino, M. Jones, T. Shiota, J. X. Qin, N. L. Greenberg, L. A. Cardion, A. J. Morehead, A. D. Zetts, A. Travaglini, F. Bauer, J. A. Panza, and J. D. Thomas, "Real-time three-dimensional color Doppler echocardiography for characterizing the spatial velocity distribution and quantifying the peak flow rate in the left ventricular outflow tract," *Ultrasound Med. Biol.*, vol. 27, pp. 69–74, 2001.

[14] B. Firek, M. Higginbotham, S. Russel, D. Adams, C. Landolfo, and J. Kisslo, "Initial experience with volume-rendered, real-time three-dimensional echocardiography in right ventricular endomyocardial biopsy," *Eur. Heart. J.*, vol. 21, p. 3064, 2000.

[15] C. J. McCreery, M. McCulloch, M. Ahmad, and M. deFilippi, "Real-time 3-dimensional echocardiography imaging for right ventricular endomyocardial biopsy: A comparison with fluoroscopy," *J. Amer. Soc. Echocardiog.*, vol. 14, no. 9, pp. 927–933, 2001.

[16] C. E. Fleishman, J. Li, T. Ota, C. J. Ohazama, G. Stetten, D. Adams, O. T. von Ramm, and J. Kisslo, "Identification of congenital heart defects using real-time three-dimensional echo in pediatric patients," *Circulation*, vol. 94, no. Suppl. I-416, p. 2423, 1996.

[17] J. T. Yen and S. W. Smith, "Real-time rectilinear volumetric imaging," *IEEE Trans. Ultrason., Ferroelect., Freq. Contr.*, vol. 49, no. 1, pp. 114–124, 2002.

[18] L. J. Busse, C. G. Oakley, M. J. Fife, J. V. Ranalletta, R. D. Morgan, and D. R. Dietz, "The acoustic and thermal effects of using multiplexers in small invasive probes," in *Proc. IEEE Ultrason. Symp.*, 1997, pp. 1721–1724.

[19] J. T. Yen and S. W. Smith, "Real-time curvilinear and improved rectilinear volumetric imaging," in *Proc. IEEE Ultrason. Symp.*, 2001, pp. 1117–1122.

[20] J. T. Yen and S. W. Smith, "Real-time rectilinear volumetric imaging using a periodic array," *Ultrasound Med. Biol.*, vol. 28, no. 7, pp. 923–931, 2002.

[21] S. S. Brunke and G. R. Lockwood, "Broad-bandwidth radiation patterns of sparse two-dimensional vernier arrays," *IEEE Trans. Ultrason., Ferroelect., Freq. Contr.*, vol. 47, no. 3, pp. 764–770, 2000.

[22] A. Austeng and S. Holm, "Sparse arrays for 3-D phased array imaging-design methods," *IEEE Trans. Ultrason., Ferroelect., Freq. Contr.*, vol. 49, pp. 1073–1086, 2002.

[23] J. A. Jensen and N. B. Svendsen, "Calculation of pressure fields from arbitrarily shaped, apodized, and excited ultrasound transducers," *IEEE Trans. Ultrason., Ferroelect., Freq. Contr.*, vol. 39, pp. 262–267, 1992.

[24] J. O. Fiering, P. Hultman, W. Lee, E. D. Light, and S. W. Smith, "High-density flexible interconnect for two-dimensional ultrasound arrays," *IEEE Trans. Ultrason., Ferroelect., Freq. Contr.*, vol. 47, pp. 764–770, 2000.

[25] R. Krimholtz, D. A. Leedom, and G. L. Matthei, "New equivalent circuits for elementary piezoelectric transducers," *Electron. Lett.*, vol. 6, pp. 398–399, 1970.

[26] S. W. Smith, H. Lopez, and W. J. Bodine, "Frequency independent contrast-detail analysis," *Ultrasound Med. Biol.*, vol. 11, pp. 467–477, 1985.

Jesse T. Yen was born in Houston, TX, on September 23, 1975. He received B.S.E. and Ph.D. degrees in biomedical engineering from Duke University in Durham, NC, in 1997 and 2003, respectively.

He is currently an assistant professor in the Biomedical Engineering Department at the University of Southern California, Los Angeles, CA. His research interests include 2-D array design and fabrication, 3-D ultrasound, and 3-D elastography.

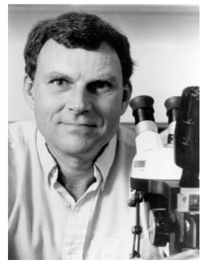

Stephen W. Smith (M'91) was born in Covington, KY, on July 27, 1947. He received the B.A. degree in physics in 1967 from Thomas More College, Ft. Mitchell, KY, the M.S. degree in physics in 1969 from Iowa State University, Ames, and the Ph.D. degree in biomedical engineering in 1975 from Duke University, Durham, NC.

In 1969, he became a Commissioned Officer in the U.S. Public Health Service, assigned to the Food and Drug Administration, Center for Devices and Radiological Health, Rockville, MD, where he worked until 1990 in the study of medical imaging, particularly diagnostic ultrasound and in the development of performance standards for such equipment. In 1978, he became an adjunct associate professor of radiology at Duke University Medical Center. In 1990, he became associate professor of biomedical engineering and radiology, and Director of Undergraduate Studies in Biomedical Engineering at Duke University.

Dr. Smith has served on the Education Committee of the American Institute of Ultrasound in Medicine, the Executive Board of the American Registry of Diagnostic Medical Sonographers, and the Editorial Board of *Ultrasonic Imaging*. He was co-recipient of the American Institute of Ultrasound in Medicine Matzuk Award in 1988 and 1990 and co-recipient of the IEEE-UFFC Outstanding Paper Award in 1983 and 1994. He holds seven patents in medical ultrasound and has authored 100+ publications in the field.